X-ray powder diffraction refinement of $PbTi_{(1-x)}Fe_xO_{(3-\delta)}$ solid solution series

Hasitha Ganegoda,[a] James A. Kaduk, and Carlo U. Segre
Department of Physics and CSRRI, Illinois Institute of Technology, Chicago, Illinois

(Received 7 January 2013; accepted 7 May 2013)

A series of iron-doped lead titanate $PbTi_{(1-x)}Fe_xO_{(3-\delta)}$ samples in the $x = 0$–1 composition range was prepared using sol–gel synthesis at a calcination temperature of 700 °C. The room temperature Cu$K\alpha$ powder diffraction data collected from $x = 0$, 0.005, 0.01, 0.025, 0.05, 0.075, 0.1, 0.125, 0.15, 0.175, 0.2, and 0.3 samples were analyzed using the Rietveld method. Magnetoplumbite ($PbFe_{12}O_{19}$) secondary phase formation was observed at compositions $x = 0.4$, 0.5, 0.6, 0.7, 0.8, 0.9, and 1. Fe-composition dependent decrease of tetragonal distortion has been observed. According to Vegard's law, the B-site iron solubility limit in the lead titanate host was found to be approximately 10 mol% ($x = 0.1$). Homogeneous distribution of dopants below the solubility limit was evidenced by the linear behavior of unit-cell parameters. The absence of a cubic phase and the persistence of distorted oxygen octahedra indicated the existence of ferroelectric properties even at the $x = 0.3$ composition. Beyond $x = 0.3$, the *P4mm* tetragonal model was determined to be invalid possibly because of oxygen defect driven structural changes, mainly tilting Fe-polyhedra. © *2013 International Centre for Diffraction Data*. [doi:10.1017/S0885715613000511]

Key words: powder structure refinement, iron-doped lead titanate, GSAS

I. INTRODUCTION

Multiferroics are materials that exhibit a combination of ferromagnetic, ferroelectric, and piezoelectric properties (Martin *et al.*, 2008). Ferroelectric materials have a wide range of applications such as non-volatile memory devices, capacitors, and precision actuators (Lines, 2001). Similarly, magnetic materials are employed in storage devices and many other applications (Handley, 2000). The co-existence of both ferroelectric and ferromagnetic properties in one material provides a fertile ground for fundamental research as well as technological applications (Eerenstein *et al.*, 2006). Materials with coupled ferroelectric and ferromagnetic order parameters provide an additional degree of freedom in device design, since polarization of the material can be switched using either the magnetic field or the electric field (Kimura *et al.*, 2003; Hur *et al.*, 2004; Tokura, 2006). This property is valuable in information storage device design, since (in theory) a data bit can be written with an electric field and read using a magnetic probe, and vice versa (Verma *et al.*, 2009). However, room temperature multiferroics are scarce, since the competing conditions are hard to satisfy simultaneously (Spaldin and Fiebig, 2005). Both ferroelectricity (reflected by lattice distortions) and ferromagnetism are related to the d-orbital occupancy (Hill, 2000). The wide range of ferroelectric perovskite materials with a ABO_3 chemical formula contain B-site cations such as Ti^{4+}, Nb^{5+}, and Zr^{4+} with empty d orbitals. Doping transition-metal cations with d-electrons reduces the tendency for an off-centering distortion, thereby reducing the lattice distortion responsible for ferroelectricity. Nevertheless, Palkar and Malik (2005) reported the existence of magneto-electric properties in a $PbTi_{0.5}Fe_{0.5}O_{(3-\delta)}$ sample, with a tetragonal distortion of 1.028. This is surprising, since a high level of Fe^{3+} substituted in Ti^{4+} site may create oxygen vacancies that lead to structural instabilities. Similar studies by Ren *et al.* (2007, 2009) and Liu *et al.* (2010) also reported room temperature ferromagnetic behavior in low Fe-doped (4 mol%) $PbTiO_3$ (PT) nanocrystals.

Ferroelectric perovskite B-site doping with 3d magnetic transition elements has been extensively studied (Kim, 2005; Koduri and Lopez, 2007; Stoupin *et al.*, 2007). Many electron paramagnetic resonance (EPR) studies have shown that magnetic ions are indeed incorporated into the B-sublattice (Dimza, 1993; Eichel, 2007; Keeble *et al.*, 2009; Puthucheri *et al.*, 2011). In an effort to better understand the $PbTi_{(1-x)}Fe_xO_{(3-\delta)}$ solid solution system (PTF), we have synthesized a series of samples using a wet chemical synthesis route followed by a moderate temperature (700 °C) calcination. In this paper, we report the structures of the PTF series up to $x = 0.3$ obtained using the Rietveld method (Rietveld, 1969). The effects of charge compensating oxygen vacancies were studied using lattice strain, the variation of B–O bond length and strain were compared against existing theoretical predictions (Meštrić *et al.*, 2005), and the solubility limit of Fe in PT has been established. Cubic, cubic + tetragonal, and tetragonal models were tested. Based on the goodness-of-fit, the existence of a cubic PTF phase at Fe concentrations $x \leq 0.3$ was ruled out. PTF samples with $x \geq 0.4$ contained an additional phase, $PbFe_{12}O_{19}$ (Diaz-Castanon *et al.*, 1998). In the perovskite structure, oxygen octahedra-encapsulated B-site cations are arranged in a corner-sharing configuration. With perovskites, the crystallographic shear

[a]Author to whom correspondence should be addressed. Electronic mail: hganegod@iit.edu

https://doi.org/10.1017/S0885715613000511 Published online by Cambridge University Press

(CS) structure, where along the CS planes the octahedra share edges or faces instead of corners and edges, is generally believed to be not realizable (Mitchell, 2002). The existence of a perovskite-based CS structure has been reported for $Pb_2Fe_2O_5$ (Abakumov *et al.*, 2006; Batuk *et al.*, 2011). The end member of our sample series, $x = 1$ contains $Pb_2Fe_2O_5$, $PbFe_{12}O_{19}$, and PbO.

II. EXPERIMENTAL

Wet chemical techniques have an advantage over conventional solid state processing in terms of higher solubility, homogeneity, and distribution of dopants (Mulla *et al.*, 2007). Our PTF samples were prepared using an acetic acid based sol–gel route. All reagents of choice, lead subacetate, Pb $(C_2H_3O_2)_2{\cdot}2Pb(OH)_2$ (Sigma-Aldrich, ACS reagent grade) iron(III) acetylacetonate, $Fe(C_5H_7O_2)_3$ (Sigma-Aldrich, 99.9%), and titanium isopropoxide $Ti(OCH(CH_3)_2)_4$ (Sigma-Aldrich 99.999%), have good solubility in the solvent, acetic acid (Thermo-Fisher 98.5%). Stoichiometric solutions with desired Fe-concentrations were prepared by dissolving appropriate amounts of precursor powders in acetic acid. Lead sub- acetate and iron(III) acetylacetonate powders were separately dissolved in small beakers using 25–35 ml of acetic acid. Complete dissolution was achieved with the aid of a magnetic stirrer. Excess amounts of lead (typically 3%) were used to compensate for possible lead volatilization (Ma *et al.*, 2009). On complete dissolution, two solutions were poured into a large beaker and stirred for approximately 10 min. Subsequently, a stoichiometric amount of titanium isopropoxide, typically between 1.25 and 5 ml was added while the solution was constantly being stirred. Ultrasonication promotes better mixing, aids gelation, and prevents pyrochlore phase formation (Kim *et al.*, 2000), therefore, the solution was ultrasonicated for 1–3 h where longer sonication times are associated with higher iron concentrations. The solution was then transferred into a Petri dish for gel formation. Drying was carried out inside a 75 °C furnace and dried samples were ground and pyrolyzed in air at 300 °C for 5 h. Samples were then re-ground and calcined in air at 700 °C for 3 h to form the crystallized powders.

X-ray diffraction (XRD) patterns were collected using a Bruker D2 PHASER diffractometer in Bragg–Brentano geometry employing Ni filtered Cu$K\alpha$ radiation. Data collection were performed from 5 to 130°2θ using a LynxEye linear position sensitive detector. A step width of 0.02°2θ and a counting time of 0.5 s step^{-1} were used. The diffractrograms were evaluated by the Rietveld method using the program EXPGUI (Toby, 2001) a graphical user interface to General Structure Analysis System (GSAS) and profile function 4 (Larson and Von Dreele, 2000). Partial occupancies of Fe and Ti were difficult to refine, and thus set to nominal composition values. Attempts to refine site occupancies of Pb or O resulted in non-physical or diverging fits, and were hence assumed to be unity. All other structural parameters of samples up to $x = 0.3$ were refined. The z-coordinates of the atomic positions were also refined, except Pb, where the coordinates were fixed at (0, 0, 0) to define the origin. Isotropic displacement coefficients (U_{iso}) of all atoms were refined up to $x = 0.2$. To increase stability of the fit, U_{iso} of Ti, Fe, and O of $x = 0.3$ sample were set to those of the $x = 0.2$ sample and the U_{iso} of Pb was refined. GSAS profile function 4 parameters such as sample displacement (shft) and all anisotropic strain broadening terms (S_{hkl}) were refined. The pseudo-Voigt mixing ratio (η) of the profile function was refined except at $x = 0.3$ where the line shape was considered Lorentzian ($\eta = 1$). Anisotropic strain in tetragonal symmetry was modeled with four S_{hkl} parameters to account for the strain induced, reflection (hkl) dependent, lineshape broadening. The correlations between crystallite size (Scherrer) broadening (LX), S_{hkl} terms, and η adversely affected the quality of the refinements, mainly above the $x = 0.05$ composition. Consequently, the LX value of PTF samples with $x = 0.075$ and beyond was assumed to be constant and held at the LX value extracted from the $x = 0.05$ refinement. The background was fitted using a six-term shifted Chebyshev polynomial function.

III. RESULTS AND DISCUSSION

The powder diffractograms of PTF samples ($x = 0$, 0.005, 0.01, 0.025, 0.05, 0.075, 0.1, 0.125, 0.15, 0.175, 0.2, and 0.3) showed that they were free of common impurity phases, such as the pyrochlore phases $Pb_2Ti_2O_6$ or $Pb_2Ti_2O_7$. A low intensity sharp peak resulting from Cu$K\beta$ leakage was observed at the low theta base of the most prominent peak. This region was not excluded and may have a small negative effect on the goodness-of-fit. All the diffraction peaks of $PbTiO_3$ were indexed using tetragonal $P4mm$ (99) symmetry (Nelmes and Kuhs, 1985) as shown in Figure 1. Rapid decrease of (001)–(100) tetragonal splitting was observed up to $x = 0.1$, after which splitting was no longer visible. Diffraction peaks of the samples in the composition range $x = 0.1$–0.3 show broadening and increased asymmetry. Samples with Fe concentration $x \leq 0.3$ are free from impurity phases. The diffractogram of $x = 0.4$ has minor reflections from the ferromagnetic magnetoplumbite phase, $PbFe_{12}O_{19}$. The intensities of these reflections increase with increasing iron concentration. A recent study (Kleebe *et al.*, 2009) reports magnetoplumbite phase formation in $Pb(Zr_{0.6}Ti_{0.4})O_3$ ceramics doped beyond the 3 mol% solubility limit with Fe^{3+} ions. The formation of magnetoplumbite could be responsible for the room-temperature ferromagnetism reported in 4 mol% Fe-doped $PbTiO_3$ nanocrystals (Ren *et al.*, 2007). The end member $x = 1$ sample contains $PbFe_{12}O_{19}$, $Pb_2Fe_2O_5$, and lead oxide (PbO), which confirms phase segregation at higher Fe-dopant concentrations. Diffractograms of the PTF sample series are shown in Figure 2.

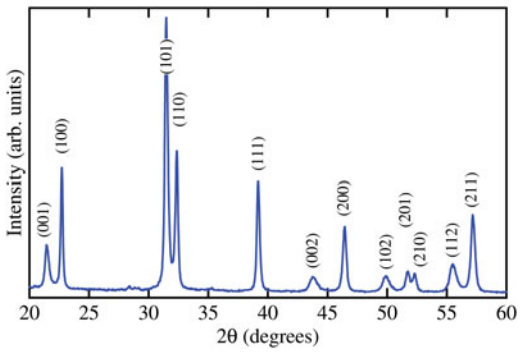


Figure 1. (Color online) Diffraction pattern of $PbTiO_3$ prepared using the sol–gel route. Diffraction peaks are indexed with a tetragonal $P4mm$ crystal structure.

https://doi.org/10.1017/S0885715613000511 Published online by Cambridge University Press

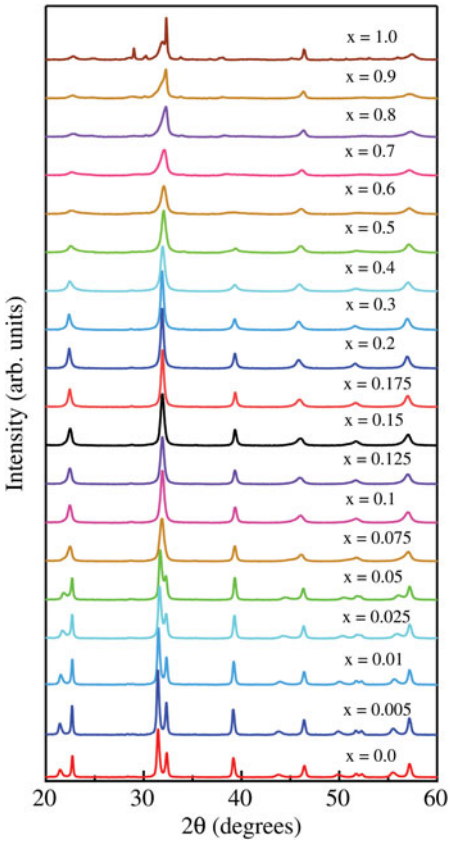


Figure 2. (Color online) Diffraction patterns of the $PbTi_{(1-x)}Fe_xO_{(3-\delta)}$ solid solution series. The evolution of the diffraction peaks indicates loss of tetragonal splitting at $x = 0.1$. Samples with $x \geq 0.4$ show diffraction peaks belonging to secondary phases, mainly $PbFe_{12}O_{19}$.

Rietveld refinements yielded goodness-of-fit (χ^2) values between 2.05 and 3.45. The profile residual (*R*p) and weighted profile residual (R_{wp}) values were in the ranges of 3.77–4.96% and 4.79–6.51%, respectively. Significantly large correlations between LX, η, and S_{hkl} parameters were observed in fits of samples with iron composition $x \geq 0.075$. Reliability of the refined parameters was improved by carefully constraining these parameters as discussed above. The line shapes changed from having more Gaussian characters to more Lorentzian characters with increased Fe concentration. Consequently, η was allowed to refine. Peak broadening and asymmetry have many different origins. Three main contributions to line shape are considered to be instrumental broadening, crystallite size broadening, and strain broadening. Strain is a measure of lattice stress existing in the material as a result of crystal imperfections. Residual stresses in PTF originate primarily from the paraelectric → ferroelectric phase transition that occurs on cooling from growth temperature (Levin *et al.*, 2007). In addition, strain contributions from oxygen vacancies, other forms of point defects, line defects, and plane defects may result in line shape broadening (Jenkins and Snyder, 1996). Several models were tested to best-fit datasets refining a minimum number of parameters. Higher quality of microstrain-containing refinements indicated the existence of strain-induced line shape broadening. The crystalline size distribution of PTF depends on sintering temperature and time duration, and is presumably less sensitive to changes in the composition. It was clear that constraining LX was more

TABLE I. Rietveld refinement fit parameters, pseudo-Voight mixing ratios, and crystallite sizes of $PbTi_{(1-x)}Fe_xO_{(3-\delta)}$ samples.

x	χ^2	R_p (%)	R_{wp} (%)	η	P (nm)
0	2.05	4.20	5.38	0.62	230.0
0.005	2.64	4.46	5.72	0.64	268.3
0.01	2.85	4.70	6.07	0.66	215.8
0.025	3.37	4.89	6.42	0.57	123.9
0.05	3.45	4.96	6.51	0.52	120.8
0.075	2.70	4.70	5.90	0.65	120.8[a]
0.1	2.52	4.41	5.50	0.71	120.8[a]
0.125	2.26	4.26	5.34	0.71	120.8[a]
0.15	2.42	4.22	5.29	0.68	120.8[a]
0.175	2.42	4.26	5.38	0.81	120.8[a]
0.2	2.09	3.77	4.79	0.91	120.8[a]
0.3	3.04	4.21	5.50	1.00	120.8[a]

[a]Held constant during refinement.

feasible than constraining η or S_{hkl}. Therefore, LX was held constant at the value of the $x = 0.05$ fit for all higher Fe concentrations. Final fit residuals, χ^2, η values, and crystallite sizes at different Fe concentrations are listed in Table I.

The *c*/*a* ratio of our $PbTiO_3$ sample, 1.056, is lower than the value 1.066 (Palkar *et al.*, 2007) reported in the literature. The linear change in unit-cell parameter, following Vegard's law (Denton and Ashcroft, 1991), is a strong indication that B-site doping is homogeneous. The sol–gel preparation technique is known to produce samples with better homogeneity and high purity at lower processing temperatures compared to traditional solid state synthesis (Mulla *et al.*, 2007). The elemental maps of Pb, Ti, and Fe show uniform dopant distribution up to $x = 0.3$. Figure 3 shows the elemental maps captured using Fe*K*α fluorescence line intensity. White arrows

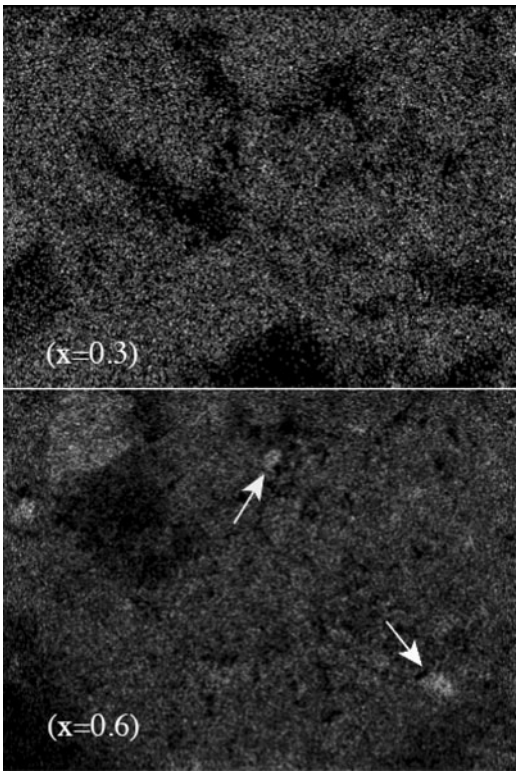


Figure 3. Elemental maps of $PbTi_{(1-x)}Fe_xO_{(3-\delta)}$, $x = 0.3$ and $x = 0.6$ samples using the Fe*K*α fluorescence line. Arrows indicate Fe-rich regions.

https://doi.org/10.1017/S0885715613000511 Published online by Cambridge University Press

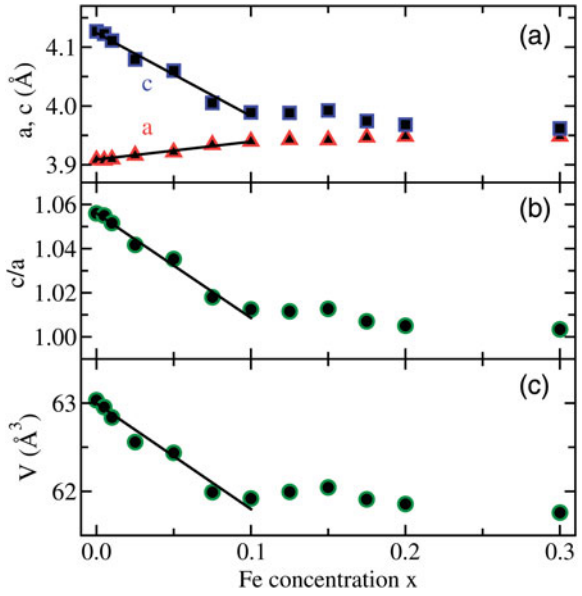


Figure 4. (Color online) Cell parameters obtained from Rietveld refinement of PTF XRD data at room temperature as a function of Fe concentration. (a) Unit-cell parameters *a* and *c*, (b) tetragonal distortion *c/a,* and (c) cell volume.

indicate Fe-rich regions that appear to be Pb-deficient in Pb elemental maps.

Rapid decrease of tetragonal distortion and the absence of XRD reflections from segregated phases support the conclusion that Fe-ions are indeed homogeneously distributed. Figure 4(a) shows that both unit-cell parameters *a* and *c* change linearly with concentration until 10 mol% ($x = 0.1$) of the B-sites are doped with Fe. Beyond $x = 0.1$, neither unit-cell parameters nor tetragonal distortion (see Figures 4 and 5) follow the same linear trend. Therefore, the solubility limit of Fe in $PbTiO_3$ host B-site using our sol–gel synthesis

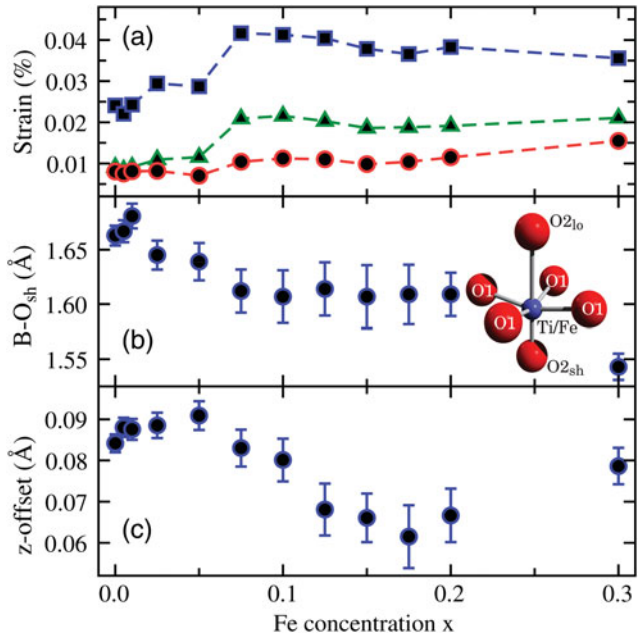


Figure 5. (Color online) As a function of Fe concentration: (a) the variation of strain in the (00*l*) (triangles), (*hk*0) (squares), and (111) (circles) planes; (b) the shortest B–O bond length (B–$O2_{sh}$); (c) the offset in the *z*-direction between the B-site cation and oxygens in *a*, *b* faces (|B(*z*)–O1(*z*)|).

method is approximately 10 mol%. The $x = 0.3$ sample has minimum tetragonal distortion. The changes in tetragonal distortion and cell volume vs. concentration are shown in Figures 4(b) and 4(c). The Wyckoff positions (*x*, *y*, and *z*) for Pb (1a), Ti/Fe (1b), O1 (2c), and O2(1b), and unit-cell constants *a*, *c* are given in Table II.

The common tetragonally distorted $PbTiO_3$ structure consists of an off-center shifted Ti^{4+} ion surrounded by six oxygen atoms. The oxygen octahedron is elongated and shifted along the *c*-direction, with respect to Pb^{2+} ions. The Pb^{2+} ions are 12-fold coordinated by oxygens and are located at the corners of the unit cell. Ti^{4+} and Fe^{3+} have similar ionic radii, 0.605 and 0.58 Å, respectively (Shannon, 1976) The ionic radius of the A-site occupying Pb^{2+}, 1.63 Å, is much larger than those of Ti^{4+} or Fe^{3+}. Consequently, Fe^{3+} is preferentially substituted at the B-site. When a Ti^{4+} is replaced by Fe^{3+}, charge compensation necessitates formation of oxygen vacancies. Density functional theory (DFT) calculations by Meštrić *et al.* (2005) using a $2 \times 2 \times 2$ $PbTiO_3$ supercell have shown that formation of oxygen vacancies along the *c*-direction is energetically more favorable than other directions. The effect of spin polarization on the energy was found to be insignificant. Furthermore, the cation nearest to the vacant site moves away from the vacancy, shortening the metal–oxygen bond distance. With homogeneously distributed dopants, the composition $x = 0.125$ corresponds to one Fe^{3+} ion substitution and nominally one-half oxygen vacancy created per $2 \times 2 \times 2$ supercell.

Modification of $PbTiO_3$ B-sites by Fe^{3+} tends to form $(Fe'_{Ti}–V_O^{\cdot\cdot})^{\cdot}$ defect dipoles with partially charge-compensated oxygen vacancies (Eichel, 2007). In this notation Fe'_{Ti} represents the negative charge created by replacing Ti^{4+} ion with Fe^{3+} in an otherwise neutral crystal structure. Similarly, $V_O^{\cdot\cdot}$ represents the doubly positive charge resulting from O^{2-} vacancy following the symbolism by Kroger and Vink (1956). $(Fe'_{Ti}–V_O^{\cdot\cdot})^{\cdot}$ defect dipoles are energetically favored to form along the polarization direction of the crystal (Meštrić *et al.*, 2005). Ideally, one oxygen vacancy could compensate two Fe'_{Ti} charges. The inclusion of vacancies in terms of oxygen partial fractions based on the Fe^{3+} concentration had no effect on the final fit, thus, oxygen occupancy was held constant at unity.

We have found that both size-type and anisotropic microstrain-type peak broadening are present in diffraction patterns. The instrument broadening effect has been parameterized using NIST SRM 660a LaB_6 standard. Anisotropic microstrain was found to be the dominant contributor to line broadening, especially at high Fe concentrations. The evolution of the size of coherently diffracting domains was refined by up to 5 mol% Fe concentration. The size of the coherently diffracting domains (assumed to be spherical) was evaluated using the Scherrer formula (Patterson, 1939):

$$P(\text{nm}) = \frac{18\,000\,K\lambda}{\pi(\text{LX} - X_{\text{inst}})}, \quad (1)$$

where $K = 0.9$ is the Scherrer constant, λ the wavelength in nanometers, X_{inst} the instrumental broadening, and LX the refined Lorentzian coefficient for size-type broadening (Larson and Von Dreele, 2000). Calculated Scherrer particle sizes are listed in Table I. The anisotropic strain broadening has been modeled using the description of Stephens

https://doi.org/10.1017/S0885715613000511 Published online by Cambridge University Press

https://doi.org/10.1017/S0885715613000511 Published online by Cambridge University Press

TABLE II. Structural parameters for $PbTi_{(1-x)}Fe_xO_{(3-\delta)}$ samples obtained by Rietveld refinement. Space group *P4mm*.

x	Cell	Atom	x	y	z	U_{iso} (Å^2)	x	Cell	Atom	x	y	z	U_{iso} (Å^2)
0	a=3.908 17(8) Å	Pb	0	0	0	0.018 32(26)	0.1	a=3.939 84(23) Å	Pb	0	0	0	0.033 65(34)
	c=4.126 88(15) Å	Ti/Fe	0.5	0.5	0.5261(15)	0.0131(8)		c=3.989 08(44) Å	Ti/Fe	0.5	0.5	0.5138(35)	0.0195(9)
	c/a=1.055 96(4) O1	O1	0.5	0	0.6102(15)	0.0093(16)		c/a=1.012 50(13)	O1	0.5	0	0.594(4)	0.0159(34)
	V=63.033(4) Å^3	O2	0.5	0.5	0.1231(17)	0.0093(16)		V=61.920(9) Å^3	O2	0.5	0.5	0.1100(35)	0.0159(34)
0.005	a=3.907 66(8) Å	Pb	0	0	0	0.023 07(27)	0.125	a=3.942 60(24) Å	Pb	0	0	0	0.0347(4)
	c=4.122 75(14) Å	Ti/Fe	0.5	0.5	0.5232(17)	0.0197(8)		c=3.988 28(45) Å	Ti/Fe	0.5	0.5	0.515(4)	0.0187(9)
	c/a=1.055 04(4) O1	O1	0.5	0	0.6113(16)	0.0145(17)		c/a=1.011 59(13)	O1	0.5	0	0.583(5)	0.028(4)
	V=62.954(4) Å^3	O2	0.5	0.5	0.1189(18)	0.0145(17)		V=61.994(8) Å^3	O2	0.5	0.5	0.110(4)	0.028(4)
0.01	a=3.909 56(9) Å	Pb	0	0	0	0.022 91(31)	0.15	a=3.942 15(21) Å	Pb	0	0	0	0.0358(4)
	c=4.111 22(16) Å	Ti/Fe	0.5	0.5	0.5239(19)	0.0191(8)		c=3.992 34(39) Å	Ti/Fe	0.5	0.5	0.517(4)	0.0180(10)
	c/a=1.051 58(5) O1	O1	0.5	0	0.6114(17)	0.0126(18)		c/a=1.012 73(11)	O1	0.5	0	0.583(5)	0.032(4)
	V=62.839(4) Å^3	O2	0.5	0.5	0.1151(19)	0.0126(18)		V=62.043(8) Å^3	O2	0.5	0.5	0.114(4)	0.032(4)
0.025	a=3.916 10(13) Å	Pb	0	0	0	0.0264(4)	0.175	a=3.946 76(29) Å	Pb	0	0	0	0.0362(4)
	c=4.079 29(22) Å	Ti/Fe	0.5	0.5	0.5184(23)	0.0212(9)		c=3.974 49(54) Å	Ti/Fe	0.5	0.5	0.519(4)	0.0139(12)
	c/a=1.041 67(6) O1	O1	0.5	0	0.6069(20)	0.0133(20)		c/a=1.007 03(16)	O1	0.5	0	0.580(6)	0.031(5)
	V=62.559(6) Å^3	O2	0.5	0.5	0.1152(22)	0.0133(20)		V=61.910(8) Å^3	O2	0.5	0.5	0.114(4)	0.031(5)
0.05	a=3.921 51(14) Å	Pb	0	0	0	0.0274(4)	0.2	a=3.948 17(28) Å	Pb	0	0	0	0.0370(4)
	c=4.060 04(23) Å	Ti/Fe	0.5	0.5	0.5154(27)	0.0220(9)		c=3.968 26(53) Å	Ti/Fe	0.5	0.5	0.521(4)	0.0167(12)
	c/a=1.035 33(7) O1	O1	0.5	0	0.6063(22)	0.0159(23)		c/a=1.005 09(15)	O1	0.5	0	0.588(5)	0.019(4)
	V=62.436(6) Å^3	O2	0.5	0.5	0.1118(24)	0.0159(23)		V=61.857(7) Å^3	O2	0.5	0.5	0.115(4)	0.019(4)
0.075	a=3.934 20(22) Å	Pb	0	0	0	0.0320(4)	0.3	a=3.948 27(36) Å	Pb	0	0	0	0.0369(4)
	c=4.005 19(38) Å	Ti/Fe	0.5	0.5	0.5172(31)	0.0196(9)		c=3.961 82(57) Å	Ti/Fe	0.5	0.5	0.5127(31)	0.016 68
	c/a=1.018 05(11) O1	O1	0.5	0	0.6003(32)	0.0150(30)		c/a=1.003 43(17)	O1	0.5	0	0.5914(32)	0.019 24
	V=61.992(10) Å^3	O2	0.5	0.5	0.1149(31)	0.0150(30)		V=61.760(10) Å^3	O2	0.5	0.5	0.1233(32)	0.019 24

(Stephens, 1999). Microstrain-type broadening in this model is considered a manifestation of the distribution of reciprocal unit-cell parameters. This distribution can originate from crystalline defects such as oxygen vacancies or local inhomogeneities in chemical composition. The microstrain along the direction [*hkl*] has been calculated according to the relationship (Stephens, 1999; Larson and Von Dreele, 2000):

$$\frac{\delta d_{hkl}}{d_{hkl}} = \frac{\pi(\sigma(M_{hkl}))^{1/2}}{18\,000 M_{hkl}}, \quad (2)$$

where $M_{hkl} = 1/d_{hkl}^2$ and σ^2 (M_{hkl}) is the variance of M_{hkl}. Complete description of the model can be found elsewhere (Stephens, 1999). In tetragonal symmetry, the strain broadening contribution to the width of the diffraction peak (*hkl*) is parametrized by (Stephens, 1999; Toby, 2001):

$$\sigma^2(M_{hkl}) = S_{400}\,(h^4 + k^4) + S_{004}\,l^4 + 3S_{220}(h^2k^2) + 3S_{202}\,(h^2l^2 + k^2l^2). \quad (3)$$

GSAS profile function 4 (Larson and Von Dreele, 2000) has been utilized to refine S_{hkl} coefficients, S_{400}, S_{004}, S_{220}, and S_{202}. The values of parameters *S*400 and *S*202 are significantly different from the others, suggesting that the crystallite strain is indeed anisotropic. The *S*202 parameter values are negative, thus variation of *a* and *c* unit-cell parameters has a negative correlation. Anisotropic strain contains useful information about "soft" crystal direction with respect to composition variations. Formation of $(Fe'_{Ti}–V_O^{\cdot\cdot})^{\cdot}$ defect dipoles upon iron doping could build up extra forces that elevate the level of strain anisotropy. Figure 5(a) shows the variation of lattice strain along different crystal directions, which represents the quantitative correlation between the magnitude of the strain and the Fe^{3+} concentration. Since the number of oxygen vacancies formed is proportional to *x*, strain can also be linked to the preferred directions of vacancy formation. Since the $(Fe'_{Ti}–V_O^{\cdot\cdot})^{\cdot}$ defect dipole is singly positive, simple electrostatic stability conditions would also require the closest oxygen ions to move toward each other, causing strain. Other mechanisms such as an electron (e′) trapped in the vacancy site could potentially satisfy the charge compensation requirements. Oxygen vacancy centered oxygen–oxygen and B-site cation–cation displacements induce strain in the lattice planes. Dissimilar ionic radii, Fe^{3+} being 0.025 Å smaller than Ti^{4+}, could also play a role in increasing strain proportional to the Fe-concentration. Anomalous increase of strain in all directions at Fe concentrations about the solubility limit may originate from structural defects. The (111) crystal planes of $PbTiO_3$ are unaffected by tetragonal distortion evidenced by the non-splitting diffraction peak. Throughout the PTF series, strain in the (111) planes remains small compared to all other directions. The differences in tetragonality between unit cells containing Ti^{4+} and Fe^{3+} ions, and formation of oxygen vacancies preferentially along the *c*-direction may have contributed to the comparatively large strain in the (*hk*0) crystal planes.

The change in short B–O bond length in the *c*-direction ($B–O2_{sh}$) vs. Fe concentration is shown in Figure 5(b). In the inset, short and long bond length oxygens are labeled $O2_{lo}$ and $O2_{sh}$, respectively. The decrease in $B–O1_{sh}$ bond length below the solubility limit is in agreement with theoretical calculations (Meštrić *et al.*, 2005). The bond length remains unchanged for $0.1 \le x \le 0.2$ but shows a large decrease at $x = 0.3$, possibly suggesting the incipient failure of the *P*4*mm* model. The four oxygen atoms on the *a* and *b* faces (labeled O1 in Figure 5(b) inset) have different *z*-coordinates than the B-cation because of ferroelectric polarization. The *z*-coordinate offset between B-cation and O1 oxygens decreases when the unit cell becomes more centrosymmetric. The offset decreases as shown in Figure 5(c) and remains non-zero even at Fe concentration $x = 0.3$. Therefore, all analyzed samples possess displacive type ferroelectric properties.

A large number of oxygen vacancies could force oxygen octahedra to shift from corner-sharing to edge-sharing or even face-sharing configurations, where a tetragonal model would no longer apply. Tilted Fe polyhedra break long-range periodicity in crystalline material. Formation of segregated phases could result in ferroelectric, Ti-rich phases and ferromagnetic, Fe-rich phases in PTF powders. The magnetoplumbite impurity phase observed in $x \ge 0.4$ samples contains both edge-sharing and face-sharing type Fe polyhedra. Local structure probes such as Pair Distribution Function (PDF) analysis or X-ray Absorption Spectroscopy (XAS) can be particularly useful in detecting the Fe concentration at which tilted Fe polyhedra are formed. Employing XAS may be particularly useful in determining the elemental specific average local structures.

The isotropic displacement coefficients (U_{iso}) were constrained such that all oxygen ions have the same value. Similarly, Ti and Fe ion U_{iso} parameters were constrained and refined in the fit. The behavior of the U_{iso} parameters was tested against different particle size broadening models and trends were verified to be similar. Figure 6 shows the refined U_{iso} parameters against Fe-composition.

U_{iso} parameters of Pb systematically increase with increasing Fe concentration. This trend may have dominant non-thermal contributions from elevated disorder or lead loss. The B-site U_{iso} parameter increases at lower concentrations ($x < 0.05$) and decreases afterwards. Any increase in U_{iso} of B-site cations or oxygen anions may have

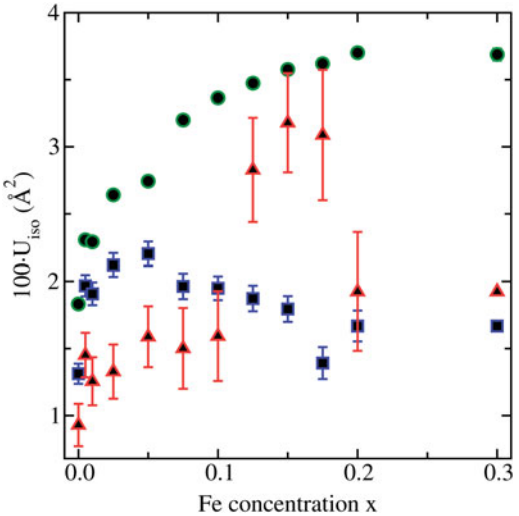


Figure 6. (Color online) Isotropic displacement coefficients, U_{iso}, multiplied by 100 for Pb (circles), Ti/Fe (squares), and O (triangles) vs. Fe concentration.

https://doi.org/10.1017/S0885715613000511 Published online by Cambridge University Press

significant partial contributions arising from disorder. At higher concentrations, B-site ions are more tightly bound to oxygen anions as evidenced by the decrease in B–O bond length. Tightly bound atoms result in reduced unit cell volume and lower U_{iso} values. Furthermore, the oxygen octahedron encapsulating the B-site cation is clearly asymmetric, thus treating thermal factors as isotropic is likely to be an invalid approximation, particularly at higher Fe-concentrations. In addition, the number of oxygen vacancies (increasing with Fe-concentration) was ignored in the refinement, and may contribute to the anomalous behavior (above the solubility limit) of the oxygen U_{iso} parameter.

IV. CONCLUSION

Samples of $PbTi_{(1-x)}Fe_xO_{(3-\delta)}$ (PTF) with $0 \le x \le 1$ were prepared using a sol–gel synthesis route. X-ray diffractograms of samples up to $x = 0.3$ indicate a perovskite ABO_3 structure, free of impurities such as pyrochlore phases or iron oxides. PTF samples with $x \ge 0.4$ have secondary phases, mainly $PbFe_{12}O_{19}$. The end member ($x = 1$) consists of $PbFe_{12}O_{19}$, $Pb_2Fe_2O_5$, and lead oxide (PbO). The results obtained from Rietveld refinement of these data using a B-site composition-based $PbTiO_3$ tetragonal (*P4mm*) model show a rapid decrease in the *c* unit-cell parameter and a slow increase in the *a* unit-cell parameter with increasing Fe concentration. The decrease in tetragonal distortion is expected to result in a reduction of ferroelectricity with increasing Fe-dopant concentration.

The linear variation of PTF unit-cell parameters on Fe-concentration persists up to $x = 0.1$, the B-site Fe^{3+} solubility limit using our sol–gel synthesis technique, subjected to a maximum sintering temperature of 700 °C. These results suggest that the Fe dopants are homogeneously distributed only up to $x \approx 0.3$. In contrast, Palkar's $PbTi_{0.5}Fe_{0.5}O_{(3-\delta)}$ sample (Palkar and Malik, 2005) shows clear evidence of (001)–(100) tetragonal splitting. This sample was prepared at 1000 °C which is 300 °C higher than our processing temperature. Therefore, the splitting of diffraction peaks at $x = 0.5$ could be the result of phase segregation where a Ti-rich phase remains tetragonally distorted.

Formation of charge compensating oxygen vacancies, hence $(Fe'_{Ti}–V_O^{\cdot\cdot})^{\cdot}$ defect dipole formation upon B-site Fe^{3+} substitution is consistent with the previous EPR (Eichel, 2007; Erdem *et al.*, 2010) and theoretical (Meštrić *et al.*, 2005) investigations. The creation of oxygen vacancies in the *c*-direction at the O-site furthest from B-site Fe^{+3} is energetically favorable (Meštrić *et al.*, 2005). The strain in the *c*-direction is distinctly higher as a result of inhomogeneities in tetragonality and additional contributions from oxygen voids formed in the (*hk*0) planes. Formation of oxygen vacancies at $O2_{lo}$ sites and the lowering of $B–O2_{sh}$ bond length with Fe doping are consistent with theoretical predictions (Meštrić *et al.*, 2005). The decrease of B–O bond length with Fe concentration resulted in lower *U*iso (B) parameters. Distorted oxygen octahedra with off-center shifted B-site cation imply the continued existence of displacive type ferroelectric properties. Defect dipole formation may contribute to enhanced ferroelectric properties.

ACKNOWLEDGEMENT

This work was supported by the National Science Foundation under grant no. DMR-0806935.

Abakumov, A. M., Hadermann, J., Bals, S., Nikolaev, I. V., Antipov, E. V., and Van Tendeloo, G. (**2006**). "Crystallographic shear structures as a route to anion-deficient perovskites," Angew. Chem. **118**, 6849–6852.

Batuk, D., Hadermann, J., Abakumov, A., Vranken, T., Hardy, A., Van Bael, M., and Van Tende- loo, G. (**2011**). "Layered perovskite-like $Pb_2Fe_2O_5$ structure as a parent matrix for the nucleation and growth of crystallographic shear planes," Inorg. chem. **50**, 4978–4986.

Denton, A. R. and Ashcroft, N. W. (**1991**). "Vegard's law," Phys. Rev. A **43**, 3161–3164.

Diaz-Castanon, S., Sanchez, Ll J., Estevez-Rams, E., Leccabue, F., and Watts, B. (**1998**). "Magneto-structural properties of $PbFe_{12}O_{19}$ hexaferrite powders prepared by decomposition of hydroxide-carbonate and metal-organic precipitates," J. Magn. Magn. Mater. **185**, 194–198.

Dimza, V. I. (**1993**). "EPR studies of Mn, Fe, Co, and Cu doped PLZT and PMN compositions," Phys. Status Solidi a **140**, 543–551.

Eerenstein, W., Mathur, N. D., and Scott, J. F. (**2006**). "Multiferroic and magnetoelectric materials," Nature **442**, 759–765.

Eichel, R. -A. (**2007**). "Defect structure of oxide ferroelectricsvalence state, site of incorporation, mechanisms of charge compensation and internal bias fields," J. Electroceram. **19**, 11–23.

Erdem, E., Kiraz, K., Somer, M., and Eichel, R. (**2010**). "Size effects in Fe^{3+}-doped $PbTiO_3$ nanocrystals – formation and orientation of $(Fe'_{Ti}–V_O^{\cdot\cdot})^{\cdot}$ dipoles," J. Eur. Ceram. Soc. **30**, 289–293.

Handley, R. (**2000**). *Modern Magnetic Materials: Principles and Applications* (Wiley, New York).

Hill, N. A. (**2000**). "Why are there so few magnetic ferroelectrics?" J. Phys. Chem. B **104**, 6694–6709.

Hur, N., Park, S., Sharma, P. A., Ahn, J. S., Guha, S., and Cheong, S. (**2004**). "Electric polarization reversal and memory in a multiferroic material induced by magnetic fields," Nature **429**, 392–395.

Jenkins, R. and Snyder, R. L. (**1996**). *Introduction to X-ray Powder Diffractometry* (John Wiley & Sons Inc., New York).

Keeble, D. J., Loyo-Menoyo, M., Booq, Z. I. Y., Garipov, R. R., Eremkin, V. V., and Smotrakov, V. (**2009**). "Fe^{3+} defect dipole centers in ferroelectric $PbTiO_3$ studied using electron paramagnetic resonance," Phys. Rev. B **80**, 1–7.

Kim, J., Kim, N., and Park, B. (**2000**). "Effects of ultrasound on perovskite phase developments, microstructures, and dielectric properties of sol-gel-processed $PbTiO_3$ thin films," Inorg. Mater. **5**, 4995–4999.

Kim, K. (**2005**). "The effect of Cr doping on the microstructural and dielectric properties of $(Ba_{0.6}Sr_{0.4})TiO_3$ thin films," Thin Solid Films **472**, 26–30.

Kimura, T., Goto, T., Shintani, H., Ishizaka, K., Arima, T., and Tokura, Y. (**2003**). "Magnetic control of ferroelectric polarization," Nature **426**, 55–58.

Kleebe, H., Lauterbach, S., Silvestroni, L., Kungl, H., Hoffmann, M. J., Erdem, E., and Eichel, R. A. (**2009**). "Formation of magnetic grains in ferroelectric $Pb[Zr_{0.6}Ti_{0.4}]O_3$ ceramics doped with Fe^{3+} above the solubility limit," Appl. Phys. Lett. **94**, 142901.

Koduri, R. and Lopez, M. (**2007**). "Influence of Mn on dielectric and piezoelectric properties of A-site and B-site modified PLZT nano-ceramics for sensor and actuator applications," J. Mater. Sci.: Mater. Electron. **19**, 669–675.

Kroger, F. A. and Vink, H. J. (**1956**). *Solid State Physics*, Vol. **3**(Academic Press, New York).

Larson, A. C. and Von Dreele, R. B. (**2000**). *General Structure Analysis System (GSAS)*, Technical Report (Report LAUR 86-748). Los Alamos National Laboratory.

Levin, I., Slutsker, J., Li, J., Tan, Z., and Roytburd, A. L. (**2007**). "Accommodation of transformation strains in transverse multiferroic nanostructures $CoFe_2O_4$–$PbTiO_3$," Appl. Phys. Lett. **91**, 062912.

Lines, M. (**2001**). *Principles and Applications of Ferroelectrics and Related Materials* (Clarendon Press/Oxford University Press, Oxford/New York).

Liu, Z., Ren, Z., Wei, X., Xiao, Z., Hou, X., Shen, G., Xu, G., and Han, G. (**2010**). "Improved room-temperature ferromagnetism in self-assembled

https://doi.org/10.1017/S0885715613000511 Published online by Cambridge University Press

disk-like superstructures of Fe-doped $PbTiO_3$ nanocrystals," J. Am. Ceram. Soc. **4**, 1–4.

Ma, B., Narayanan, M., Tong, S., and Balachandran, U. (**2009**). "Fabrication and characterization of ferroelectric PLZT film capacitors on metallic substrates," J. Mater. Sci. **45**, 151–157.

Martin, L. W., Crane, S. P., Chu, Y., Holcomb, M. B., Gajek, M., Huijben, M., Yang, C., Balke, N., and Ramesh, R. (**2008**). "Multiferroics and magnetoelectrics: thin films and nanostructures," J. Phys.: Condens. Matter **20**, 434220.

Meštrić, H., Eichel, R., Kloss, T., Dinse, K., Laubach, S., Laubach, S., Schmidt, P., Schonau, K., Knapp, M., and Ehrenberg, H. (**2005**). "Iron-oxygen vacancy defect centers in $PbTiO_3$: Newman superposition model analysis and density functional calculations," Phys. Rev. B **71**, 1–10.

Mitchell, R. H. (**2002**). *Perovskites Modern and Ancient* (Almaz Press, Thunder Bay, Canada).

Mulla, I., Natarajan, N., Gaikwad, A., Samuel, V., Guptha, U., and Ravi, V. (**2007**). "A coprecipitation technique to prepare $CoTa_2O_6$ and $CoNb_2O_6$," Mater. Lett. **61**, 2127–2129.

Nelmes, R. and Kuhs, W. (**1985**). "The crystal structure of tetragonal PbTiO3 at room temperature and at 700 K," Solid State Commun. **54**, 721–723.

Palkar, V. and Malik, S. (**2005**). "Observation of magnetoelectric behavior at room temperature in $Pb(Fe_xTi_{1x})O_3$," Solid State Commun. **134**, 783–786.

Palkar, V. R., Purandare, S. C., Gohil, S., John, J., and Bhattacharya, S. (**2007**). "Scanning probe imaging of coexistent ferromagnetism and ferroelectricity at room temperature," Appl. Phys. Lett. **90**, 172901.

Patterson, A. L. (**1939**). "The scherrer formula for x-ray particle size determination," Phys. Rev. **56**, 978–982.

Puthucheri, S., Pandey, P. K., Gajbhiye, N. S., Gupta, A., Singh, A., Chatterjee, R., and Date, S. K. (**2011**). "Microstructural, electrical, and magnetic properties of acceptor-doped nanostructured lead zirconate titanate," J. Am. Ceram. Soc. **94**, 3941–3947.

Ren, Z., Xu, G., Wei, X., Liu, Y., Hou, X., Du, P., Weng, W., Shen, G., and Han, G. (**2007**). "Room-temperature ferromagnetism in Fe-doped $PbTiO_3$ nanocrystals," Appl. Phys. Lett. **91**, 063106.

Ren, Z., Xu, G., Wei, X., Liu, Z., Wang, Y., Xiao, Z., Shen, G., and Han, G. (**2009**). "Ring- and single-crystal-like superstructures of Fe-doped $PbTiO_3$ nanocrystals," J. Cryst. Growth **311**, 4593–4597.

Rietveld, H. M. (**1969**). "A profile refinement method for nuclear and magnetic structures," J. Appl. Crystallogr. **2**, 65–71.

Shannon, R. D. (**1976**). "Revised effective ionic radii and systematic studies of interatomic distances in halides and chalcogenides," Acta Crystallogr. Sect. A **32**, 751–767.

Spaldin, N. A. and Fiebig, M. (**2005**). "Materials science. The renaissance of magnetoelectric multiferroics," Science **309**, 391–392.

Stephens, P. W. (**1999**). "Phenomenological model of anisotropic peak broadening in powder diffraction," J. Appl. Crystallogr. **32**, 281–289.

Stoupin, S., Chattopadhyay, S., Bolin, T., and Segre, C. (**2007**). "High concentration manganese doping of ferroelectric $PbTiO_3$," Solid State Commun. **144**, 46–49.

Toby, B. (**2001**). "EXPGUI, a graphical user interface for GSAS," J. Appl. Crystallogr. **34**, 210–213.

Tokura, Y. (**2006**). "Multiferroics as quantum electromagnets," Science **312**, 1481–1482.

Verma, K. C., Kotnala, R., and Negi, N. (**2009**). "Intrinsic study for magnetoelectric coupling in nanoparticles," Solid State Commun. **149**, 1743–1748.

https://doi.org/10.1017/S0885715613000511 Published online by Cambridge University Press